



HAL
open science

Modelling the clear-sky intensity distribution using a sky imager

Rémi Chauvin, Julien Nou, Stéphane Thil, Stéphane Grieu

► **To cite this version:**

Rémi Chauvin, Julien Nou, Stéphane Thil, Stéphane Grieu. Modelling the clear-sky intensity distribution using a sky imager. *Solar Energy*, 2015, 119, pp.1-17. 10.1016/j.solener.2015.06.026 . hal-01273096

HAL Id: hal-01273096

<https://univ-perp.hal.science/hal-01273096>

Submitted on 11 Feb 2016

HAL is a multi-disciplinary open access archive for the deposit and dissemination of scientific research documents, whether they are published or not. The documents may come from teaching and research institutions in France or abroad, or from public or private research centers.

L'archive ouverte pluridisciplinaire **HAL**, est destinée au dépôt et à la diffusion de documents scientifiques de niveau recherche, publiés ou non, émanant des établissements d'enseignement et de recherche français ou étrangers, des laboratoires publics ou privés.



Distributed under a Creative Commons Attribution - NonCommercial - NoDerivatives 4.0 International License

Modelling the clear-sky intensity distribution using a sky imager

Rémi Chauvin^a, Julien Nou^a, Stéphane Thi^{a,b}, Stéphane Grieu^{a,b,*}

^aPROMES-CNRS (UPR 8521), Rambla de la thermodynamique, Tecnosud, 66100 Perpignan, France

^bUniversité de Perpignan Via Domitia, 52 Avenue Paul Alduy, 66860 Perpignan, France

Abstract

This paper introduces a new empirical formulation of the clear-sky intensity distribution based on images acquired with a sky imager developed at the PROMES-CNRS laboratory (Perpignan, France). Both the formulation and image processing methodology are detailed and stand for key steps in the development of a high quality cloud detection algorithm. The work presented in this paper is a part of a research project which aims at improving solar plant control procedures using direct normal irradiance forecasts under various sky conditions at short-term horizon (5-30 min) and high spatial resolution ($\sim 1 \text{ km}^2$). Modeling the clear-sky intensity distribution in real time allows clear-sky images to be generated. These clear-sky images can then be used to remove the clear-sky background anisotropy on images and so improve cloud detection algorithms significantly. Cloud detection is essential in short-term solar resource forecasting. The new formulation is especially designed for improving performance of the existing models in the circumsolar area. When tested over more than 2200 clear-sky images, corresponding to a solar zenith angle spanning from 24° to 85° , the new formulation outperforms a standard approach based on the All-Weather model (Perez et al., 1993) by 15% on the whole sky and more than 20% in the circumsolar area. Application of the methodology for the real-time cloud detection purpose is discussed at the end of the paper.

Keywords: sky-imaging system, clear-sky intensity distribution, circumsolar radiation, cloud detection.

Nomenclature

PAA	Pixel/Azimuth or Point/Azimuth Angle ($^\circ$)
PZA	Pixel/Zenith or Point/Zenith Angle ($^\circ$)
SAA	Sun/Azimuth Angle ($^\circ$)
SZA	Sun/Zenith Angle ($^\circ$)
SPA	Sun/Pixel or Sun/Point Angle ($^\circ$)
NRBR	Normalized Red/Blue Ratio
L_p	Luminance distribution (cd m^{-2})
l_r	Relative luminance distribution
$R_{p,\lambda}$	Spectral radiance distr. ($\text{W m}^{-2} \text{ nm}^{-1} \text{ sr}^{-1}$)
R_p	Radiance distribution ($\text{W m}^{-2} \text{ sr}^{-1}$)
r_r	Relative radiance distribution
E_p	Irradiance reaching the CMOS sensor (W m^{-2})
I_p	Pixel intensity in the sensor coordinate system
I_p^*	Pixel intensity in the (PZA,SPA) coord. system
Ω_p	Pixel solid angle (sr)
Ω_{cone}	Solid angle of a cone (sr)
f	Scattering function
b_i	Coefficients of the scattering function
ϕ	Gradation function
a_i	Coefficients of the gradation function
CS_p	Generated clear-sky image

1. Introduction

It is widely acknowledged by solar companies and plant operators that cost remains the main drawback of Concentrating Solar Power (CSP) systems. In that context, the project CSPIMP (Concentrated Solar Power efficiency IMProvement) has been initiated in 2013 in order to make CSP plants more competitive. Among the different challenges pointed out by this research project, the solar resource assessment and forecasting are essential tasks since they would allow a better real-time management of the solar field, and thus reduce the maintenance activities, while improving the expected benefits. As a consequence, a sophisticated solar resource forecasting model is under development at PROMES-CNRS in order to deal with the plant's behaviour against solar variability. This model will take advantage of a sky-imaging system allowing the cloud cover and the cloud motion to be measured at high spatial and high temporal resolution. Regarding the cloud cover estimation, classical thresholding techniques are widely used due to their simplicity and their ability to identify cloud pixels at low computational cost. However, such techniques suffer from the anisotropy of the clear-sky background. Indeed, with classical thresholding techniques, the circumsolar area and the Sun are systematically identified as clouds, whereas thin clouds are often identified as clear-sky pixels. Therefore, removing the clear-sky anisotropy from sky images would significantly improve the cloud detection algorithm. The present paper is dedicated to this issue.

First, a review of the existing sky radiance and luminance distribution models is presented (Section 2). Their potential use for

*Corresponding author

Email address: stephane.grieu@promes.cnrs.fr (Stéphane Grieu)

our application is also discussed. The next section gives some details about the sky-imaging systems and focuses especially on both the experimental setup and the camera angular calibration (Section 3). Section 4 introduces the clear-sky intensity distribution function developed for our application. Section 5 is about results, remarks and discussion. The paper ends with a conclusion and an outlook to future work.

2. History and development of sky standards

This section provides extended information about the sky radiance and luminance distribution models developed up to now. First, a few applications of such distributions are given. Then, a review of radiative transfer models and empirical models is presented. Finally, the potential of measuring the distribution using a sky-imaging system is discussed.

2.1. Applications of sky radiance/luminance distribution

Sky radiance and luminance distributions have been studied for many years in architecture to improve buildings' design according to the daylight availability (Vartiainen, 2001; Reinhart and Walkenhorst, 2001; Lehar and Glicksman, 2007). Indeed, the knowledge of these distributions is an important input of ray-tracing models simulating the thermal and luminous indoor environment of buildings. Optimizing the windows' sizes and orientations, for instance, could potentially reduce the buildings energy consumption and has shown strong positive effects on human psyche (Heschong, 2002; van Bommel and van den Beld, 2004). Studies dealing with sky radiance distribution have been also carried out in the field of solar collectors in order to compute the incident energy on inclined surfaces and improve the design of CSP or photovoltaic systems (Siala and Hooper, 1990; Vartiainen, 2000). Finally, because the sky radiance mainly depends on the aerosols properties, measuring this radiance distribution can provide information about the atmospheric particles, like their size distribution, the scattering phase function or the single scattering albedo. As a result, inversion algorithms have been developed in order to retrieve some aerosol optical properties based on measurements or estimation of the sky radiance distribution (Dubovik and King, 2000; Olmo et al., 2008). For these reasons, monitoring and quantifying the daylight availability has become increasingly important during the last decades and have motivated the scientific community to search for a comprehensive and scalable model of the sky radiance/luminance distribution under various sky conditions.

2.2. Radiative transfer models

The sky radiance distribution can be obtained accurately using atmospheric radiative transfer models (Liang and Lewis, 1996; Kocifaj, 2009, 2012, 2015). These models are based on the total optical thickness of the atmosphere, the scattering ability of atmospheric layers and also the reflectance of underlying surface. In a plan-parallel atmosphere, the radiative transfer equation can be solved exactly and provides a physically well-founded spectral model of the sky radiance distribution. The sky

luminance distribution L_p is then obtained as follows (Eq. (1)):

$$L_p = K_M \int_{380\text{ nm}}^{780\text{ nm}} R_{p\lambda} V(\lambda) d\lambda \quad (1)$$

where $K_M = 683 \text{ lm W}^{-1}$ is a conversion constant, $R_{p\lambda}$ is the spectral radiance distribution, and V is a luminous efficiency function corresponding to the daylight spectral response of the human eye. Although L_p can be computed as the integral product of $R_{p\lambda}$ and $V(\lambda)$, it has been experimentally observed that sky radiance and luminance distributions have similar angular behaviours, even though they do not correspond quantitatively. Consequently, these distributions have already been modeled using the same equation but with different sets of free parameters (Igawa et al., 2004; Kocifaj, 2009).

When solving the radiative transfer equation, a detailed knowledge of the physical and chemical composition of the atmosphere is required. Although some simplifying assumptions can be used, a physically-correct model would involve at least basic aerosol parameters, such as the aerosol optical depth and the aerosol scattering phase function. Unfortunately, aerosol properties happen to be highly variable in both space and time, as well as difficult to measure (Gueymard, 2012). Moreover, a spectral analysis of the sky is currently not wished for our application and the radiative transfer models are notoriously time-consuming to use. Consequently, such models are not suitable for a real-time cloud detection application and a simpler model is needed.

2.3. Empirical models

Resulting from the facts mentioned above, alternative approaches using empirical formulas fitted on observed sky radiance/luminance data have been developed. One of the first detailed measurements of the diffuse sky radiance anisotropy was developed by Steven (Steven, 1977), who measured the sky radiance at 34 points in the sky dome for a range of solar zenith angles going from 30° to 60° . However, he was not able to fit a good analytical expression to these data. Following Steven's work, Harrison (Harrison and Coombes, 1988) developed an analytic formula based on a greater number of sampled sky directions, a wider range of solar zenith angles, and a shorter scanning time. Harrison put forward the clear-sky radiance symmetry about the solar meridian. He showed that sky radiance is minimal in the solar meridian at about 100° from the Sun and does not significantly depend on the aerosol optical depth. At that time, in the late 1980s, early 1990s, many other empirical models dealing with the sky radiance and luminance distributions were developed (Gueymard, 1986; Perez et al., 1990; Harrison, 1991; Brunger and Hooper, 1993). This boost coincided with the establishment of the IDMP stations network (International Daylight Measurement Program) by the CIE (Commission Internationale de l'Éclairage) in 1991. This network aims at measuring the visible Sun radiation (400 to 800 nm) in order to understand and model the variation of daylight. IDMP stations measure horizontal and vertical illuminances and apply to their data a quality control procedure defined by the CIE (CIE, 1994). Note that in all these models, sky elements close to the Sun were systematically excluded from the development of the empirical

formulas. Indeed, this area was removed because the authors were looking for the diffuse sky radiance/luminance without any contamination from the direct sunlight. The diffuse sky radiance in the circumsolar area is simply extrapolated afterwards, using the model fitted on the other parts of the sky. Discussion about the impact of this extrapolation on our application is provided in Section 4.2 of the paper.

Nevertheless, Perez undertook an experimental evaluation of the different models existing at that time and concluded that there was some room for improvement. He developed an ‘All-Weather model’, a new empirical model of the sky luminance distribution (Perez et al., 1993), accounting for the systematic directional errors remaining in the existing models. According to this model, the luminance L_p of a sky element can be computed using Eq. (2):

$$L_p = l_r L_z \quad (2)$$

where L_z is the zenith luminance and l_r is the relative luminance, defined as the ratio of the luminance of a sky element to the zenith luminance (Eq. (3)):

$$l_r = \frac{\phi(\text{PZA})f(\text{SPA})}{\phi(0)f(\text{SZA})} \quad (3)$$

where PZA is the Point/Zenith Angle, SPA the Sun/Point Angle, and SZA the Solar/Zenith Angle (see Figure 1).

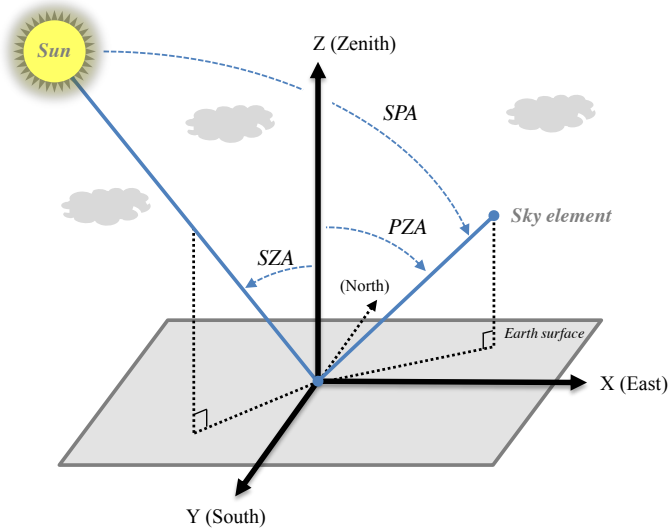


Figure 1: View of the zenith angles and the scattering angle.

In Eq. (3), the function ϕ is traditionally named the gradation function and formulates the luminance angular behaviour upon the zenith angle PZA. The function f is named the scattering function and is associated to the direct sunlight scattered by air molecules (Rayleigh theory) and aerosols (Mie theory). It can be noticed that the dependence of the relative luminance distribution l_r upon PZA and SPA has been splitted in two functions. This separation originates from the solution of the radiation transfer equation for a very clean atmosphere in a single scattering approximation (Van de Hulst, 1980; Kocifaj, 2009). Indeed, in a cloudless atmosphere, the intensity contribution of multiple

scattered light decreases rapidly and no more than three scatterings are usually considered. Under cloudy conditions, the effect of multiple scattered light can however be significant and splitting the relative luminance in two functions might produce high errors (Adamson, 1975; Kocifaj, 2015). Nevertheless, since the objective of this work is rather to attenuate the clear-sky background dependence upon zenith angle and Sun position than to estimate the clear-sky image perfectly, it is not senseless to consider only the first scattering order and use the separation variable strategy. The consequences of this strong assumption are discussed in detail in Section 5.3, where clouds come to influence the clear-sky pattern. It must be pointed out that there is also an exception, in clear-sky atmosphere, for sky elements close to the Sun. In this area, the sky radiance distribution is strongly dependent on aerosols and a rigorous Mie theory should be used instead of the empirical formulation. This is another reason why current empirical models do not consider the circumsolar area (see discussion in Section 4.2).

In the All-Weather model developed by Perez, functions ϕ (Eq. (4)) and f (Eq. (5)) are defined as:

$$\phi(\text{PZA}) = 1 + a_1 \exp\left(\frac{a_2}{\cos(\text{PZA})}\right) \quad (4)$$

$$f(\text{SPA}) = 1 + b_1 \exp(b_2 \text{SPA}) + b_3 \cos^2(\text{SPA}) \quad (5)$$

The coefficients $\{a_1, a_2\}$ and $\{b_1, b_2, b_3\}$ are functions of the solar zenith angle SZA, the sky clearness ϵ , and the clearness brightness Δ , as defined by Perez (Perez et al., 1983). These coefficients are firstly derived from Eq. (3) using a non-linear least-squares fitting on a large number of luminance measurements. Then, the coefficients are correlated to SZA and Δ through an analytical equation that is discrete in terms of ϵ . The discretization upon ϵ led to a classification of the sky into eight categories, from a very clear sky to a fully overcast sky. This model has the advantage to be usable for all kind of sky conditions without any prior knowledge of the luminance sky condition. In the late 1990s, Darula and Kittler defined a new set of fifteen standard skies made from specific combinations of six different sets of coefficients for the gradation function and six other sets for the scattering function (Kittler et al., 1997). This model also uses Eq. (3) with the same gradation function and a slightly modified scattering function (Eq. (6)):

$$f(\text{SPA}) = 1 + b_1 \left[\exp(b_2 \text{SPA}) - \exp\left(\frac{b_2 \pi}{2}\right) \right] + b_3 \cos^2(\text{SPA}) \quad (6)$$

The motivation of Kittler was to represent a wider range of skies, e.g. quasi-clear, quasi-cloudy or bright overcast skies, depending on the cloud patterns and atmospheric turbidity. In 2003, the CIE published a report (CIE, 2003) where the fifteen standards skies developed by Darula and Kittler were adopted as the new CIE Standard General Sky. This Standard defines a set of outdoor daylight conditions linking sunlight and skylight for both theoretical and practical purposes and is a universal basis for the classification of measured sky luminance distributions. The values of the coefficients used for the fifteen standard skies can

Table 1: Overview of the database specifications used in the development of some empirical models.

	Steven (1977)	Harrison et al. (1988)	Perez et al. (1993)	Kittler et al. (1997)	Igawa et al. (2004)
Sky model	Radiance	Radiance	Luminance	Luminance	Radiance & luminance
Location(s)	United Kingdom	Canada	USA	USA & Japan	Japan
Period(s)	06/1975–05/1976	07/1983–03/1986	06/1985–12/1986	06/1985–12/1986 03/1992–09/1993 01/1994–12/1994	03/1992–09/1993 01/1994–12/1994
Scanning time	40 min	12 min	n/a	n/a & 3.5 min	3.5 min
Time step(s)	n/a	20 min	15 min	15 min & 30 min	15 min & 30 min
# of scans	67	3166	15929	15929 & 829	829
Clear-sky scans	67	3166	4803	4803 & 172	172
Points per scan	34	144	186	186 & 145	145
SZA	[30°,60°]	[28°,80°]	n/a	n/a & [20°,70°]	[20°,70°]
PZA	[30°,75°]	[0°,83°]	n/a	n/a & [0°,84°]	[0°,84°]
SPA	n/a	SPA > 10°	n/a	n/a & SPA > 15°	SPA > 15°
Sky type	Clear-sky	Clear-sky	8 sky types	15 sky types	Continuous

be found in (Kittler et al., 1998; CIE, 2003). One can note that, in building applications, alternative approaches of sky model blends were also developed in order to extend the capabilities of existing ‘narrow-range’ models. For instance, it has been shown that simple blends of the CIE overcast, CIE clear and intermediate models may be adequate to improve prediction of time-varying sky luminance patterns (Mardaljevic, 2008).

After this CIE Standard update, the only significant model that was developed is the Igawa model (Igawa et al., 2004)). It is based on Eq. (3), using the scattering function developed by Kittler, i.e. Eq. (6). The main contribution of the Igawa model, compared to previous models, is its ability to estimate both the sky radiance and luminance distributions for a unique standard sky. It means that the concept of a set of standard skies, existing in the Perez and CIE models through the discrete values of the coefficients in Eqs. (4) and (5) or (6), is replaced by a unique standard sky with continuously varying coefficients. These coefficients are functions of a sky index S_i , defined as a combination of a clear-sky index K_C and a cloudless ratio C_{le} . That improvement should reduce luminance prediction errors in case of skies falling between two standard skies. In a recent analysis, Ferraro compares the ability of the Perez, CIE and Igawa models to predict the sky luminance distribution that he measured (Ferraro et al., 2012). He shows that the best results are found using the CIE model. However, when luminance is not measured, it is not possible to use this model. Indeed, the main problem arising with the CIE Standard is that no criterion, with the exception of luminance measurements, exists to establish which standard sky must be used. Unfortunately, classical meteorological stations do not measure luminance whereas solar radiation is daily measured. On the other hand, Perez and Igawa have developed a sky criterion, respectively ϵ and S_i , that is function of the diffuse, direct and global irradiance. Thus, when luminance data are not available, sky conditions can still be estimated using the Perez or the Igawa model. According to Ferraro

(Ferraro et al., 2012), the Igawa method is more accurate for the prediction of the absolute irradiance while the Perez method is more accurate for the prediction of the relative luminance. More recently, Igawa released an improved version of its previous model (Igawa, 2014), but no extensive evaluation of this model has been performed yet. Table 1 summarizes the specifications of the databases used during the models development.

2.4. Sky luminance/radiance distribution measurement using a sky imager

As said before, the empirical models have been developed using measured data of the sky radiance and luminance across the whole sky. These measurements were performed with a photometer or a spectroradiometer mounted on a tracker. Depending on the studies, about one hundred points, evenly distributed across the sky, were recorded during each scan. The main problem of such a technique is the instrument response time for each complete sky scan (see Table 1). For instance, a sky scanner like the MS-321LR Sky Scanner, developed by Eko Instruments, is able to scan the whole sky (145 points) in about 4.5 min. This scanning time is a problem since atmosphere may change between two consecutive measurements at different viewing angles. Moreover, a sky scanner is costly and data are only available in few locations.

On the other hand, cameras equipped with a fisheye lens have the ability to deliver very high resolution images of the whole sky and are much less expensive. Moreover, a color camera would even be able to deliver broadband maps of the sky radiance. However, the trade-off with such a system is the high complexity to set up and calibrate the camera, hereafter named the sky imager, and then to process automatically the data obtained. Nevertheless, in the recent years, several tries have been initiated in order to measure the sky radiance and luminance distributions using a sky imager. In 2007, Rossini developed an experimental system able to simultaneously supply images from

the sky, obtained from a commercial monochromatic CCD camera, and solar irradiance data (Rossini and Krenzing, 2007). He mainly demonstrated the feasibility of measuring the relative sky radiance and luminance distributions using a sky imager. In 2012, another study (Román et al., 2012) proposed a new methodology to obtain absolute sky radiance from sky images at three wavelengths. The deviation between the spectral radiance estimated with their camera and the one measured with a sunphotometer was lower than 15%, with the exception of high scattering angles and in the circumsolar area. More recently, Tohsing also measured the sky radiance and luminance distributions with a sky imager (Tohsing et al., 2013, 2014). He compared the luminance obtained with the camera and a spectroradiometer and found a deviation below 20% for solar zenith angles less than 80° and for all sky conditions. Similar results were found for the spectral sky radiance distribution.

2.5. Summary

To conclude this section, it must be remembered that the sky radiance and luminance distributions depend on the zenith angle PZA and the angle SPA between the Sun and the considered sky element. Both distributions have similar behaviour and so they can be formulated using the same equation. Empirical models have the advantage, over radiative transfer models, of not requiring complex atmospheric data as well as being fast and easy-to-use. Up to now, the best empirical sky model is the CIE Standard General Sky if luminance data are available, and the Perez or Igawa model otherwise. The sky radiance/luminance distribution is currently measured using a sky scanner. However, this device is costly and slow to operate. A new alternative, which is under development, is based on sky-imaging systems. Although these systems are much more complex to operate, they have the potential to provide distribution maps with high temporal and spatial resolution.

The goal of this study is to generate clear-sky maps from various sky images in order to remove the background anisotropy and so improve our cloud detection algorithm. Consequently, the following parts of this paper only focus on the relative distribution of the clear-sky pixel intensity on the images. It is clear that a photometric or a radiometric calibration of our sky imager would lead to the luminance or the radiance distribution of the sky; however this is not the topic of this study.

3. Considerations about sky imagers

This section provides information about sky imagers and the angular calibration process. First, an overview of the existing sky imagers and their current applications is given. Then, our experimental setup is presented. Finally, the calibration process, needed to get the zenith and azimuth angles of every pixel, is detailed.

3.1. Review of sky imagers

Among the existing commercial sky imagers, the most known is the Total Sky Imager developed by Yankee Environmental

Systems. It uses a hemispherical mirror to reflect the sky hemisphere into a downward-pointing camera. Other industrial sky imagers exist, such as the SRF-02 and the VISJ1006 cameras, respectively developed by EKO Instruments and Schreder CMS. However, these commercial solutions suffer from a low camera resolution and limited possibilities of customization, preventing any improvement specific to our application needs. On the other hand, many customized solutions have been considered in research applications, using non-commercial sky imagers. One of the first major systems is the Whole Sky Imager developed since the 1980s (Shields et al., 2013) for military applications by the Atmospheric Radiation Measurement Climate Research Facility. This system is able to detect clouds during daytime and night-time thanks to very sophisticated algorithms with accurate detection of haze, thin clouds, and opaque clouds. Nevertheless, a system with such qualities is expensive and, as a consequence, other research laboratories have developed cost-effective alternative systems based on a camera equipped with a fisheye lens and protected by a weatherproof enclosure (Pfister et al., 2003; Marquez and Coimbra, 2011). Among them, we find the Whole Sky Camera, developed by the University of Girona (Long et al., 2006), the All-Sky Imager developed at the University of Granada (Cazorla Cabrera, 2010) or the sky imager developed by the University of California, San Diego (UCSD) (Yang et al., 2014). The UCSD Sky Imager (USI) seems to be the most advanced system. It is specifically designed for the short-term forecasting of solar irradiance. It involves high quality components associated with sophisticated algorithms. The USI is able to provide a cloud map of the studied location, allowing the forecast of ramp events for large solar plants. However, according to their developers, a large part of improvement is still possible, both in technical and scientific terms (Yang et al., 2014). Nevertheless, the works published by these laboratories are encouraging and they motivated PROMES-CNRS to get involved in this challenging topic. Consequently, an experimental unit has been installed on the laboratory roof in 2013 in order to develop a customized forecasting tool.

3.2. PROMES-CNRS sky imager

PROMES-CNRS decided to build its own system, fully customizable both from a hardware and software point of view. This decision has been motivated by the fact that all the existing sky imagers suffer from drawbacks and PROMES-CNRS believes that a custom solution would make such systems more attractive. After a detailed review of the different cameras proposed by manufacturers, a 5-megapixel camera with a color CMOS sensor has been selected. A color sensor is essential, since red and blue channels are used in the cloud detection algorithm. It also provides spectral information about the clear-sky radiance distribution. The camera, named 5481VSE-C and provided by IDS-imaging, is equipped with a Fujinon fisheye lens and protected by a waterproof enclosure manufactured by autoVimation (Figure 2). A CMOS sensor has been preferred to a CCD one because, in the CCD structure, charge flows in the direction where pixels are read, whereas in CMOS sensors the readout is performed locally at each pixel. It results that CMOS sensors are inherently more resilient to smear effect and blooming near the



Figure 2: PROMES-CNRS sky imager and a few snapshots.

Sun area. Moreover, the camera is simple and easy to setup and operate thanks to its on-board video server that offers an intuitive browser-based interface. It is also easy to integrate thanks to the power supplied via Ethernet and the minimal memory requirements because of the MJPEG data compression format. Images are collected every 20 seconds at a resolution of 1920 x 2560 pixels, with 8 bits per channel. Finally, the PROMES-CNRS sky imager is not equipped with a solar occulting device which is frequently used to reduce the light intensity reaching the sensor. Indeed, although this device improves the sky visibility by reducing pixel saturation, it occults the circumsolar area, which provides vital information concerning the very short-term solar irradiance fluctuations. To sum up, the advantages of our system over standard sky imagers include high quality components, a high sensor resolution, a robust build, a small form factor, and a full programmability.

3.3. Camera calibration

A geometric angular calibration of the camera has been performed in order to get the relationship between a given pixel on the image and its projection onto the unit sphere. The OcamCalib toolbox (Scaramuzza et al., 2006) has been used to calibrate the camera. It allows the camera to be easily calibrated through two steps. First, pictures of a checkerboard in different positions and orientations are taken (Figure 3). Then, an automatic corner extraction is performed and a linear least-squares minimization method is used to fit these points with a four-order polynomial. After the calibration process, the mean error between measured and estimated checkerboard corner positions is about 1.78 pixels. The Fujinon fisheye lens has an equidistant projection function. It means that there is a linear relationship between the incidence angle, *i.e.* the zenith angle PZA, and the distance r , in pixels, from the center of the optical system. According to our camera calibration, we found an angular resolution $dPZA/dr \approx 0.087^\circ/\text{pixel}$ (Figure 3). As a consequence, the

mean absolute error of the pixel/zenith angle is around 0.154° . This error can be compared to the apparent diameter of the Sun, which is close to 0.533° , depending on the season. A perfect Sun on the image would be represented by a disc with a diameter slightly above 6 pixels. Note that, due to saturation and blooming effects in the circumsolar area, the observed Sun is much larger. However, in the cloud detection context, sky objects with apparent diameters as small as the Sun must be detected. It is reasonable to expect detecting objects having a diameter around 6 pixels. This is the main reason why a 5-megapixel camera is needed for our application and why the error obtained after calibration is acceptable.

Once the camera is calibrated, it is possible to calculate the Pixel/Zenith Angle (PZA) and the Pixel/Azimuth Angle (PAA) for every pixel on the image, assuming that the camera is pointing the zenith. However, this last assumption is generally not met: in reality, the camera is not perfectly aligned with the zenith. Thus, during operating time, a second calibration is automatically performed daily, using the Sun position: since the misalignment with the zenith produces an incorrect detection of the Sun on the image, the camera orientation can be corrected by comparing the real position of the Sun with its position on the image. The real position of the Sun is calculated using the SG2 algorithm (Blanc and Wald, 2012), whereas the position of the Sun on the image is computed using the circular Hough transform. Finally, from a set of theoretical and real points acquired throughout the day, the optimal rotation matrix is calculated by minimizing the root mean square deviation between the two sets of points. The mean absolute error between the SG2 zenith angle and the Sun zenith angle calculated on the image, after correction, is close to 0.281° . This error has been calculated using a set of 1300 points acquired throughout a clear-sky day.

Once the angular calibration of the sky imager is performed, it is possible to get the Sun position on the image at any moment, even during cloudy days (Figure 4). The calibration also enables

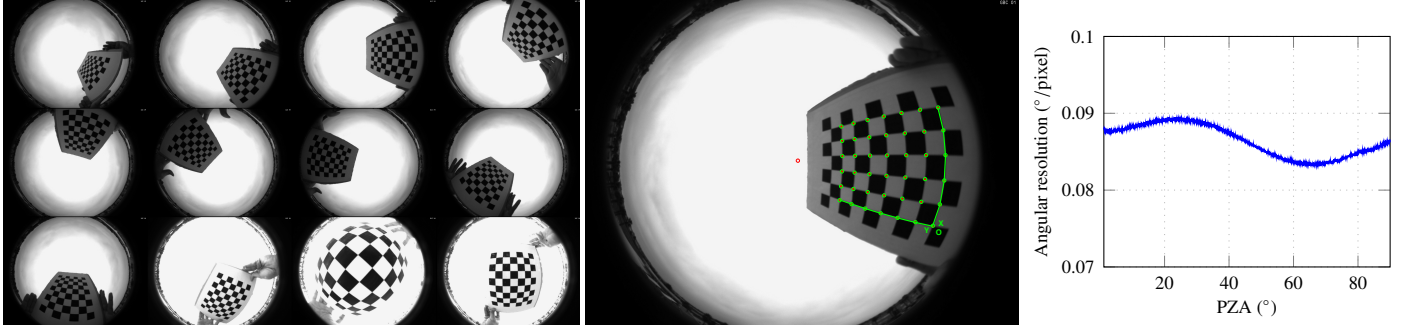


Figure 3: PROMES-CNRS sky imager calibration and the resulting angular resolution.

the PZA and PAA maps, which give the zenith and azimuth angle of every pixel on the image, to be created. Thanks to these two maps and using both the Solar/Zenith Angle (SZA) and Solar/Azimuth Angle (SAA) calculated using SG2, it is possible to create the Sun/Pixel Angle (SPA) map, defined as (Eq. (7)):

$$\cos(\text{SPA}) = \cos(\text{SZA}) \cos(\text{PZA}) + \sin(\text{SZA}) \sin(\text{PZA}) \cos(|\text{SAA} - \text{PAA}|) \quad (7)$$

The camera is now ready for studying the clear-sky pixel intensity distribution as a function of both PZA and SPA.

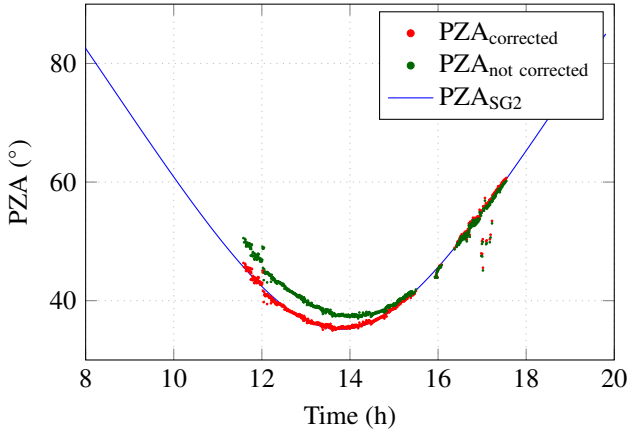


Figure 4: Sky imager calibration based on the Sun position.

4. Formulation of the clear-sky pixel intensity distribution

In this section, the proposed clear-sky pixel intensity distribution function is detailed. First, the relationship between sky radiance and pixel intensity is discussed. Then, the new formulation is presented.

4.1. From pixel intensity to scene radiance

The PROMES-CNRS sky imager delivers 8-bit color images of the full sky hemisphere. It means that the irradiance received by the camera sensor is digitized into a pixel intensity $I_p \in [0; 255]$. We found that 256 intensity levels are enough to capture the whole sky radiance up to 7° from the Sun, using our sky imager with the optimal exposure time. Note that a future improvement would be to extend the dynamic range of the camera so as to be able to measure sky radiance for $\text{SPA} < 7^\circ$ while keeping a good dynamic in the dark parts of the sky. However, the current system already allows to estimate the sky radiance at smaller SPA than previous studies (see Table 1).

Assuming a linear response function of the camera, the irradiance reaching the sensor is proportional to pixel intensity. It must be pointed out that this assumption is often not met when pixels are under- or overexposed, or when nonlinear mapping operations are performed during the acquisition process. In addition, many noise sources, both temporal (dark current and readout noise) and spatial (photo-response non-uniformity), introduce uncertainties in the conversion from pixel intensity to image irradiance. Consequently, a radiometric calibration should be performed on the camera to evaluate the relationship between pixel intensity and image irradiance. However, as mentioned before, this study is focusing on the relative distribution of the clear-sky pixel intensity, not on the scene radiance absolute value. Furthermore, tests revealed that, except for low intensity and near saturation, the camera response function is almost linear. That is why a linear response function is assumed hereafter and noise sources are neglected. The quality of the results validates this approach.

From the conservation of flux, the irradiance E_p reaching the sensor through an ordinary ideal optic follows a power of the cosine of the view angle (Smith, 2000) (Eq. (8)):

$$E_p \propto R_p \cos^4 \text{PZA} \quad (8)$$

where R_p is the sky radiance. However, due to their specific projection function, fisheye lenses are exempt to the ‘dreaded’ \cos^4 law. Instead, for an ideal fisheye lens following an equidistant projection, the irradiance E_p reaching the sensor can be expressed as (Miyamoto, 1964) (Eq. (9)):

$$E_p \propto R_p \frac{\sin \text{PZA}}{\text{PZA}} \propto R_p \Omega_p \quad (9)$$

where Ω_p is the solid angle subtended by the pixel p . Note that Eq. (9) is only valid for an ideal lens; the actual roll-off effect of our sky-imaging system might not follow that equation exactly. Again, a calibration should be performed to determine the impact of the fisheye on the incoming radiant flux carefully (Voss and Zibordi, 1989). However, previous calibration studies of sky-imaging systems have shown that the roll-off effect was determined almost wholly by the Ω_p factor (Voss and Zibordi, 1989; Juan and Da-Ren, 2009). Consequently, the relationship between the sky radiance R_p and the irradiance E_p reaching the sensor is assumed to obey Eq. (9) in this study.

Mapping the pixel solid angle Ω_p can be achieved thanks to the geometric angular calibration of the camera. Indeed, calibrating the camera provides the position of each pixel onto a unit sphere. Thus, the area S_p occupied on this sphere by the pixel p can be computed. The pixel solid angle Ω_p is then equal to S_p , since the distance d between that pixel and the center of the sphere is equal to 1 ($\Omega_p = S_p/d^2$). The pixel solid angle as a function of PZA has been plotted on Figure 5. It can be observed that pixels near the zenith have a higher solid angle than pixels near the horizon.

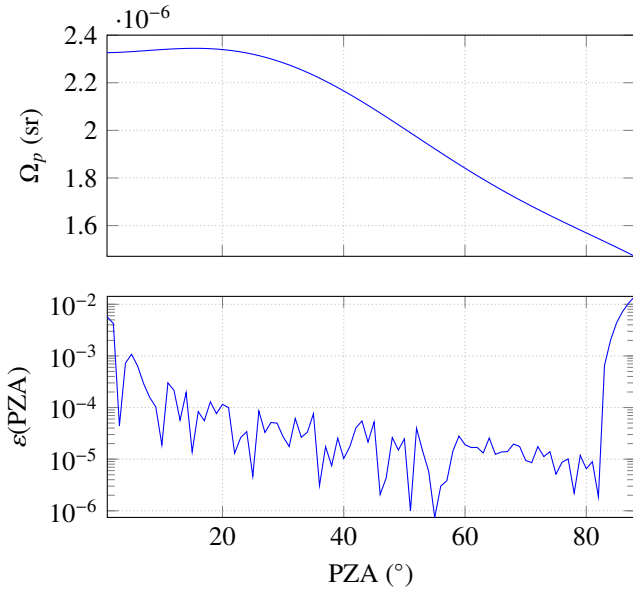


Figure 5: Solid angle and its relative error as a function of PZA.

The correctness of the map can be evaluated by summing the pixels’ solid angles over the entire hemisphere. This sum should be equal to 2π . However, as it can be seen on Figure 4, there are missing pixels on the top and bottom parts of the sky image. It results that the entire hemisphere is not visible on the image.

To overcome this issue, one solution is to sum the solid angles of pixels belonging to a reduced spherical cap, centered on the zenith, and compare the result with the solid angle subtended by a cone centered on the zenith and having the same apex angle. The solid angle of a cone centered on the zenith with half apex angle PZA is given by Eq. (10):

$$\Omega_{\text{cone}}(\text{PZA}) = 2\pi(1 - \cos(\text{PZA})) \quad (10)$$

Let $\Lambda(x)$ be the set of pixels having a zenith angle less or equal to x . Then, the sum of the pixels’ solid angles should be equal to $\Omega_{\text{cone}}(\text{PZA})$. In order to compare these two solid angles, the relative error ε between them has been calculated using Eq. (11), with $p \in \Lambda(\text{PZA})$:

$$\varepsilon(\text{PZA}) = \frac{|\Omega_{\text{cone}}(\text{PZA}) - \sum_{p \in \Lambda(\text{PZA})} \Omega_p|}{\Omega_{\text{cone}}(\text{PZA})} \quad (11)$$

The results are shown on Figure 5. One can remark that:

- ε decreases with PZA, except for high values of PZA. The decrease is due to the pixels distribution on the camera sensor: the more PZA increases, the more the perimeter drawn by pixels belonging to $\Lambda(\text{PZA})$ truly looks like the base of a cone. Conversely, a unique pixel has a solid angle closer to the solid angle subtended by a four-sided pyramid than the one subtended by a cone.
- As expected, due to the missing parts of the hemisphere in the sky image, ε rises steeply for high values of PZA, even though the error remains quite low (e.g. $\varepsilon(90^\circ) \simeq 1\%$).

Nevertheless, the most relevant relative error is computed just before the error rise and is about 0.001% at $\text{PZA} \simeq 80^\circ$.

It has been said earlier that, for an ideal optical system, the image irradiance is proportional to the scene radiance (cf. Eq. (9)). Table 2 summarizes the relationship between scene radiance and pixel intensity. As mentioned in Section 2.2, relative radiance distribution r_r and relative luminance distribution l_r can be formulated using the same type of equation, i.e. Eq. (3). It means that r_r can be expressed as a function of both the zenith angle and the scattering angle between the Sun and the sky element. In addition, the relative and absolute scene radiances, respectively r_r and R_p , are also connected through the equation $R_p = r_r R_z$, where R_z is the zenith radiance. Finally, pixel intensity I_p is proportional to image irradiance which is proportional to the scene radiance R_p multiplied by the solid angle Ω_p , subtended by the pixel p , if noise sources are neglected. It is deduced that pixel intensity I_p is proportional to the gradation and scattering functions (Eq. (12)):

$$I_p \propto \Omega_p R_p \propto \Omega_p r_r \propto \Omega_p \phi(\text{PZA}) f(\text{SPA}) \quad (12)$$

REMARK

A fisheye lens, due to its broad-view angle, is prone to vignetting effects which consist in a reduction of the image brightness when approaching the lens edges (Smith, 2000). An optical calibration would be appropriate to eliminate this effect because it might influence the relative distribution of pixel intensity, especially near

Table 2: From scene radiance to pixel intensity.

	Scene radiance	Fisheye lens	Irradiance reaching the CMOS sensor	Camera electronics	Pixel intensity
Symbol	R_p		$E_p \propto \Omega_p R_p$		I_p
Units	$\text{W m}^{-2} \text{sr}^{-1}$		W m^{-2}		–
Type	Analog		Analog		Digital

the horizon. However, such a calibration is complex, whereas the vignetting error seems insignificant on our fisheye lens. Consequently, vignetting effects are neglected in this study. Once again, the results' quality will validate that decision. ■

4.2. New formulation of the clear-sky pixel intensity distribution

According to Eqs. (4), (5), and (12), pixel intensity I_p can be formulated as follows (Eqs. (13) and (14)):

$$I_p = K\Omega_p\phi(\text{PZA})f(\text{SPA}) \quad (13)$$

$$I_p = K\Omega_p \left[1 + a_1 \exp\left(\frac{a_2}{\cos(\text{PZA})}\right) \right] \times \left[1 + b_1 \exp(b_2\text{SPA}) + b_3 \cos^2(\text{SPA}) \right] \quad (14)$$

where K is a scaling coefficient adjusting pixel intensity to the mean absolute radiance value ($K > 0$). Note that camera settings and properties, like temperature, exposure time or aperture, influence pixels' values. Nevertheless, these parameters are common for all pixels and so do not affect the relative distribution of pixels. It results that such parameters would only influence K . According to Eq. (3), K is also dependent on the Sun position. On the other hand, $\{a_1, a_2\}$ and $\{b_1, b_2, b_3\}$ are adjustable coefficients used to match Eq. (14) to the observed clear-sky pixel intensity distribution. Under clear-sky conditions, the gradation coefficient a_1 regulates the brightness intensity near the horizon whereas a_2 modulates the zenith to horizon gradient ($a_1 < 0$ and $a_2 < 0$). The vignetting effect, mentioned in Section 4.1, reduces the natural brightness near the horizon. It is deduced that coefficients $\{a_1, a_2\}$ might be underestimated. Regarding the scattering function coefficients, $\{b_1, b_2\}$ control the relative intensity and width of the circumsolar area ($b_1 > 0$ and $b_2 < 0$) whereas b_3 depicts the relative intensity of backscattered light received at the Earth's surface ($b_3 > 0$).

As mentioned in Section 2.3, sky elements close to the Sun have been often not included in the empirical models development. Indeed, when approaching the Sun position, the measured sky radiance is contaminated by the direct sunlight. However, the circumsolar area is the sky region having the highest dynamic range and contains up to 10% of the total diffuse sky radiance (Harrison and Coombes, 1988). Moreover, this area is of particular interest for our application since circumsolar clouds are very likely to influence the direct normal irradiance. Consequently, the ability of the model to represent accurately the clear-sky radiance in the circumsolar area is actually a key point.

In the past, many attempts have been made to measure the solar aureole profiles with various measuring systems, involving digital cameras, scanning photometers and telescopes (Grether et al., 1980; Neumann and von der Au, 1997; Kalapatapu et al., 2012; Wilbert et al., 2013). For low SPA values, Grether observed that the radiance profile is almost linear in log-log space, as a function of SPA, in the circumsolar region (Eq. (15)):

$$R_p = e^\kappa \text{SPA}^\delta \quad (15)$$

This observation was then confirmed during other measurement campaigns and has put forward the existence of a generic model of the circumsolar radiance distribution based on Eq. (15). In order to corroborate these past observations, some pixel intensity profiles (I_p), provided by our sky imager, have been plotted on Figure 6 as a function of SPA. Note that these profiles have been computed with a constant PZA in order to remove the zenithal dependence of I_p . It can be noted on Figure 6 that the linear relationship between I_p and SPA, in log-log space, is clear and thus validates the observation made by Grether. In 2003, Buie developed an empirical model of the radiance profile as a function of SPA and the circumsolar ratio, which is the ratio of the circumsolar radiance to the direct and circumsolar radiances (Buie et al., 2003). This model is now widely used in optical modelling of solar concentrating systems.

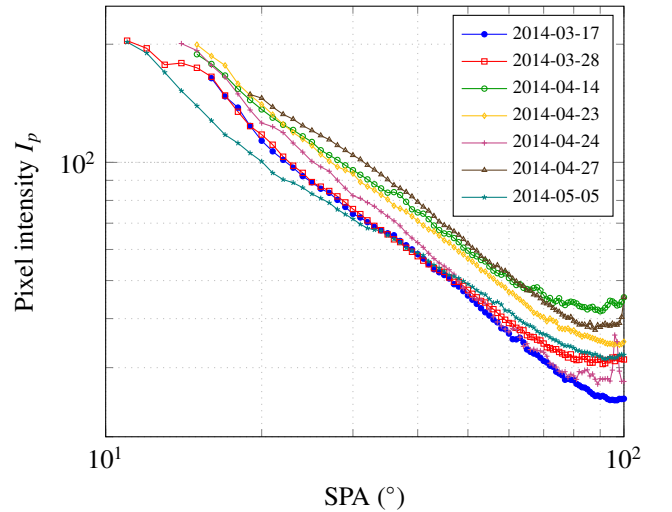


Figure 6: Pixel intensity profiles as a function of SPA for a few days of March, April, and May 2014.

Conversely, unlike the observation made by Grether, Eq. (14) exhibits an exponential dependence on the scattering function

at low SPA values (i.e. $b_1 \exp(b_2 \text{SPA})$). This exponential dependence was convenient so far, in that it allows modelling of both clear-sky and cloudy-sky radiance distributions, as long as no high resolution is needed in the circumsolar area. Indeed, it has been shown that the All-Weather model (Perez et al., 1993) largely underestimates the circumsolar ratio values when compared to literature-based values (Eissa et al., 2014), which motivates a new formulation that overcomes the limitations of Eq. (14). The scattering function f can be modified to better represent the clear-sky radiance distribution in the circumsolar area (Eq. (16)). In order to do so, it has been decided to substitute the first term of the scattering function by a logarithmic term inspired by Eq. (15):

$$f(\text{SPA}) = 1 + b_1 \text{SPA}^{b_2} + b_3 \cos^2(\text{SPA} + b_4) \quad (16)$$

Note that a fourth coefficient b_4 has been included in this new formulation. This coefficient has been added in order to reinforce the relative intensity of pixels having a large SPA value. Finally, the new clear-sky pixel intensity distribution can be formulated as follows (Eq. (17)):

$$I_p = K\Omega_p \left[1 + a_1 \exp\left(\frac{a_2}{\cos(\text{PZA})}\right) \right] \times \left[1 + b_1 \text{SPA}^{b_2} + b_3 \cos^2(\text{SPA} + b_4) \right] \quad (17)$$

5. Results and discussion

This section of the paper provides some details about the clear-sky image generation process. First, the sky intensity map used during the fitting process is introduced. Then, the ability of the fitting algorithm to accurately generate clear-sky images is tested. Finally, the use of the generated clear-sky images for the cloud detection purpose is presented.

5.1. Data pre-processing

In the existing empirical models, $\{a_1, a_2\}$ and $\{b_1, b_2, b_3\}$ are determined using correlation analysis based on irradiance measurements (see Section 2.3). Such models provide a mean instantaneous sky radiance distribution pattern for all sky conditions, disregarding the cloud distribution. However, in our application, considering the spatial distribution of clouds is essential, since Eq. (17) is only applied on clear-sky elements. Consequently, irradiance measurements are not enough to define sets of coefficients able to mimic the dynamic of realistic skies. To take into account the temporal changes in the clear-sky radiance due to clouds, a real-time fitting of Eq. (17) is performed, using a selection of clear-sky pixels collected in the last available image. However, a non-linear fitting of a two-dimensional equation, with 8 unknowns, is time-consuming. Therefore, clear-sky pixels must be selected carefully in order to reduce computation time while preserving the clear-sky dynamic range.

A first step consists in removing pixels verifying at least one of the conditions listed in Table 3. In this table, NRBR stands for Normalized Red/Blue Ratio. This feature is commonly used in cloud detection algorithms due to its ability to improve the

visual contrast between sky and clouds as well as its robustness to noise (Li et al., 2011) (Eq. (18)):

$$\text{NRBR} = \frac{R - B}{R + B} \quad (18)$$

where R and B correspond to the red and blue channel of the image, respectively. NRBR values typically span between -0.4 and 0.1 for our sky imager and the optimal threshold for cloud detection would be located around -0.1 . Consequently, removing pixels verifying $\text{NRBR} > -0.2$ is restrictive enough to ensure that no cloud remains in the clear-sky selection.

Once the unwanted pixels are removed, the remaining ones are classified according to their PZA and SPA. Indeed, as seen on Eq. (17), pixel intensity (I_p) is a function of the pixel/zenith angle PZA and the scattering angle SPA between the Sun and the pixel. For this reason, it is suitable to transform the sky images, provided in the sensor coordinate system, into a sky intensity map I_p^* in the (PZA, SPA) coordinate system (see Figure 7b). For the sake of computation time, I_p^* is generated with a mesh of 1° in both PZA and SPA directions. This operation allows the image resolution to be reduced while keeping a satisfying clear-sky dynamic range. Note that saturated pixels have not been removed from Figure 7a in order to discern the limit between the observed Sun and the clear sky. The (PZA, SPA) coordinate system allows properties that can hardly be seen directly in the original image to be highlighted. For example, in Figure 7b, it can be noticed that $\text{PZA} \approx 30^\circ$, $\text{SPA} < 110^\circ$ and that pixels are saturated at $\text{SPA} \lesssim 7^\circ$. In this example, the image is the brightest in the circumsolar area and for high PZA (corresponding to the near-horizon pixels). From a clear-sky image, generating I_p^* takes less than 1.5 s. Under cloudy conditions, the clear-sky pixel list is reduced and so I_p^* is generated much faster (see Figure 10b for example). In all cases, the computational cost is acceptable for our application since images are collected every 20 s. Finally, it happens that thin clouds or soiling still contaminate the sky intensity map, especially near the Sun. According to Eq. (17) and the sign of its coefficients, we should have the following inequality (Eq. (19)):

$$\frac{\partial I_p^*(\text{PZA}, \text{SPA})}{\partial \text{PZA}} \geq 0 \quad (19)$$

Because thin clouds and soiling appear often brighter than the expected clear sky, this inequality helps to remove the last unwanted elements remaining in I_p^* .

5.2. Analysis of the clear-sky image generation performance

The PROMES-CNRS sky imager is operational since July 2013 and has collected more than 750 000 images spread over 450 days. Today, image acquisition is still ongoing. Each time a new image is acquired, the corresponding irradiance measurements, provided by a rotating shadowband radiometer, are also collected. In addition, the cloud map and cloud velocity field, solar information (azimuth, zenith, air mass) and beam attenuation information (atmospheric turbidity, cloud index) are also computed and displayed on a real-time user interface. Therefore, although the following results are specific to the images used,

Table 3: Pixels removed from the clear-sky list (NRBR stands for Normalized Red/Blue Ratio).

Which pixels?	How?	Why?
Edges	$PZA > 80^\circ$	Pixels near horizon are contaminated by buildings or trees. The vignetting effects may also be important for large zenith angles.
Saturated or near saturation	$\max(\text{RGB}) > 240$	Saturated pixels do not provide information. Pixels near saturation are also removed due to the non-linearity of the camera response function near saturation.
Low values	$\min(\text{RGB}) < 20$	Dark noise becomes a significant part of the pixel's intensity when approaching the low boundary.
Artifacts	$\text{NRBR} > 0$	Lens flare comes from internal reflection and scattering of the light in the optical system. Pixels are generally brighter than they should be. Sometimes, one color is predominating, e.g. red spots in our case.
Clouds	$\text{NRBR} > -0.2$	A rough detection of clouds is necessary to avoid contamination of the clear-sky pixel selection. The threshold is willingly overestimated in order to ensure the correctness of the final pixel list.

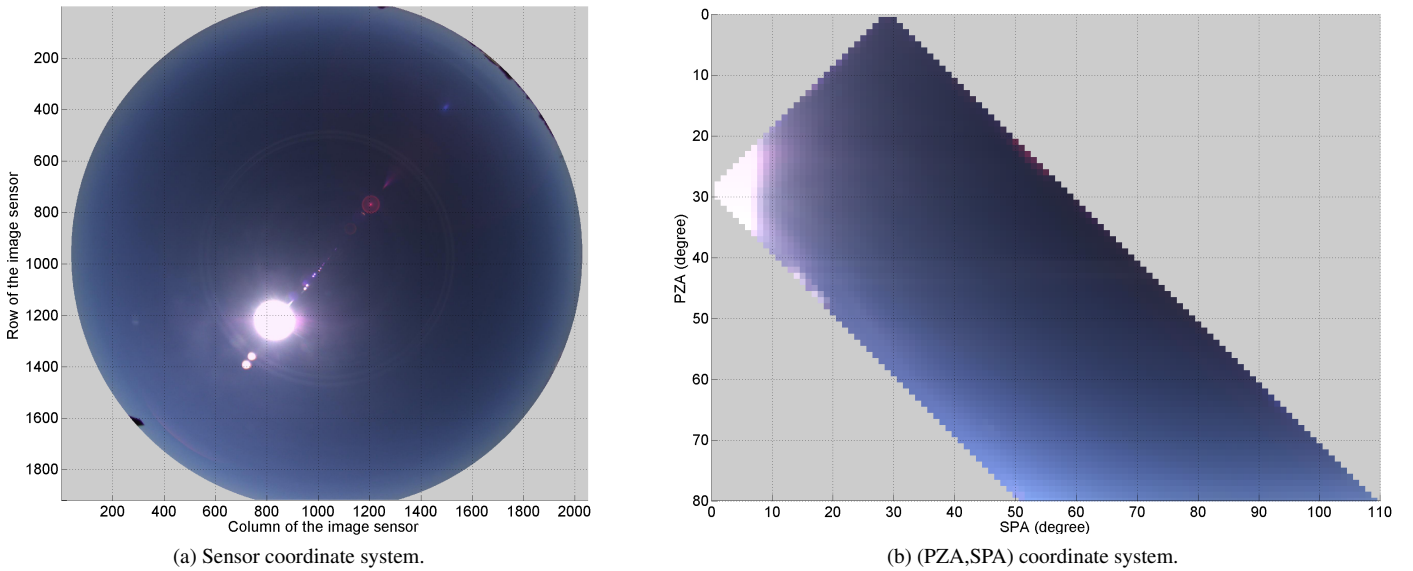


Figure 7: An example of a clear-sky image represented in the sensor coordinate system and in the (PZA,SPA) coordinate system.

the long-term monitoring of the sky has shown a good stability of these results over time (days, months and seasons). This sub-section of the paper is dedicated to the evaluation of the clear-sky image generation, which is a part of the cloud detection algorithm, using the new formulation derived in Section 4.2. The algorithm responsible for this task is named hereafter the fitting algorithm. Each time a new sky image is available, the following steps are executed:

1. Get SZA, SAA and calculate SPA (Section 3.3).
2. Upload the image and correct it using the solid angle map Ω_p (Section 4.1).
3. Pre-process the data and build I_p^* (Section 5.1).
4. Fit Eq. (14) or Eq. (17) on I_p^* (Section 4.2).
5. Generate the clear-sky image from Eq. (14) or Eq. (17).

Table 4 gives the execution time of each step and the total time. The computational cost is a strong limiting factor in our

application. Images are collected every 20 s; because we are also calculating cloud cover, cloud motion and other atmospheric properties, each step must be as fast as possible in order to get the full process below 20 s. The clear-sky image generation takes less than 4.18 s, which represents 21% of the available time. Currently, the whole process (image processing and information storage) takes around 10 s using an Intel Xeon E5-1607.

In addition, a few remarks concerning the algorithm performance are reported below:

- It takes more than 4 min to fit Eq. (14) or Eq. (17) directly on the clear-sky pixel list instead of using the pixel intensity map.
- Improving the mesh resolution of I_p^* does not improve the quality of the results while increasing the computational cost. For instance, CS_p is generated in about 13 s with a mesh of 0.25° and 6 s with a mesh of 0.5° .

Table 4: Execution time for each step.

	Execution time
Step 1	0.23 s
Step 2	0.15 s
Step 3	<1.5 s
Step 4	<0.8 s
Step 5	1.5 s
Total	<4.18 s

- If coefficients from the previous iteration are available, using them as initial values for the current iteration has proven to be very effective.
- Generating CS_p using Eq. (14) is about 30% faster than using Eq. (17).
- CS_p values are capped to 255, corresponding to the saturation level of the sky images.

In order to evaluate the accuracy of Eqs. (14) and (17), we compare a set of full clear-sky images with their corresponding generated clear-sky images CS_p . We use both the Mean Absolute Error (MAE) and the Root Mean Square Error (RMSE) as evaluation criteria:

$$MAE = \langle |I_p - CS_p| \rangle \quad (20)$$

$$RMSE = \sqrt{\langle |I_p - CS_p|^2 \rangle} \quad (21)$$

A full clear-sky day has been selected to generate clear-sky images using Eqs. (14) and (17). That day, 2279 images were acquired from 7AM to 8PM (i.e. $24^\circ < SZA < 85^\circ$), each image containing more than 3 millions of clear-sky pixels. Both MAE and RMSE between the acquired and generated images, for Eqs. (14) and (17), are presented on Figure 8. The top plot shows MAE and RMSE computed on the whole image, whereas in the bottom plot the errors have only been computed for pixels belonging to the circumsolar area (SPA $< 20^\circ$). First, we observe that MAE and RMSE remain quite low through the day, regardless of the formulation used. It can also be noticed that MAE is weakly dependent on solar elevation (i.e. the time of the day) except in the morning and late afternoon, where both MAE and RMSE slightly fluctuate. This effect is due to automatic changes in the exposure time and white balance during sunrise and sunset. As mentioned earlier, camera settings are not expected to influence that much the relative distribution of clear-sky pixels. Generally speaking, reported errors are higher using Eq. (14) than using Eq. (17). These errors, averaged over time, are given by Table 5. In this table, $\langle MAE_{20} \rangle$ and $\langle RMSE_{20} \rangle$ are respectively the mean absolute error and root mean square error in the circumsolar area, i.e. the errors computed for pixels verifying SPA $< 20^\circ$.

Using Eq. (17) on raw clear-sky images, the algorithm is able to generate clear-sky images with a mean absolute error around 2.56 pixels, that is 1% of the pixels value range. However, this error is not homogeneously distributed across the image since

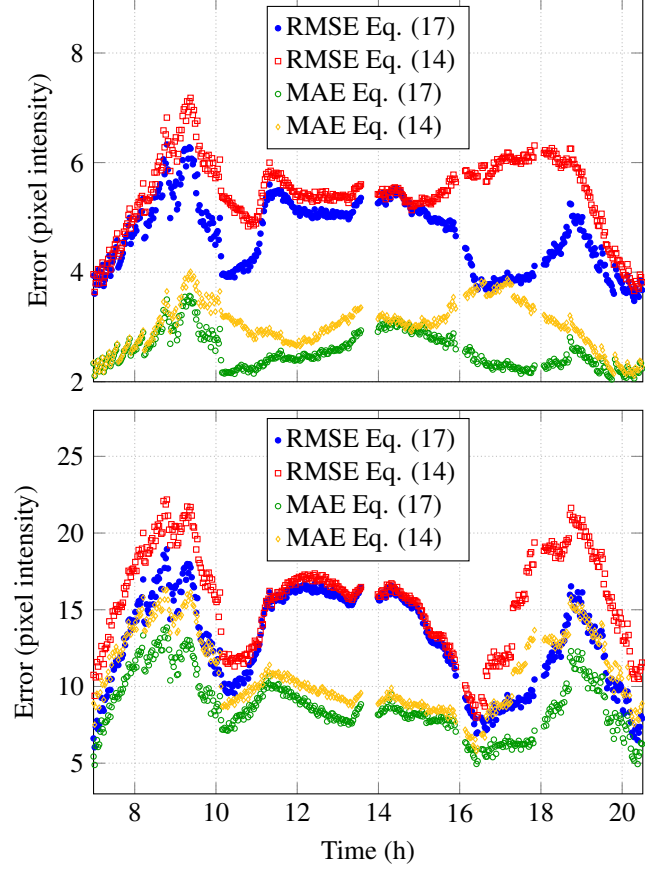


Figure 8: MAE and RMSE computed using Eq. (14) or Eq. (17), during a full clear-sky day (16th of May 2014). Top: for all pixels. Bottom: for the circumsolar area (pixels verifying SPA $< 20^\circ$).

Table 5: Mean errors averaged over time.

	$\langle MAE \rangle$	$\langle RMSE \rangle$	$\langle MAE_{20} \rangle$	$\langle RMSE_{20} \rangle$
Eq. (14)	3.02	5.44	10.89	15.72
Eq. (17)	2.56	4.69	8.71	12.99

$\langle MAE_{20} \rangle \approx 3\langle MAE \rangle$. One can observe that the most important errors are located near the Sun. It makes sense since soiling of the dome is highlighted by the Sun in this part of the image (see Figure 9). Moreover, the pixel values are higher near the Sun, meaning an absolute error potentially higher. The circumsolar area is also supposed to be the region where the difference between the two equations is the most manifest. Indeed, the main change between Eq. (14) and Eq. (17) concerns the first term of the scattering function which regulates the relative intensity and width of the circumsolar region.

According to Table 5, we improved $\langle MAE \rangle$ by 15% using the new formulation whereas $\langle MAE_{20} \rangle$ has been improved by 20%. It confirms that the improvement is especially focused on the circumsolar region. One part of the error can be explained by the camera noises, the artifacts, the soiling of the dome, and the blooming effects. However, their respective contributions are difficult to evaluate. Nevertheless, because RMSE is almost twice as big as MAE, we can expect that some outlier values are present. These outlier values are mostly related to artifacts and

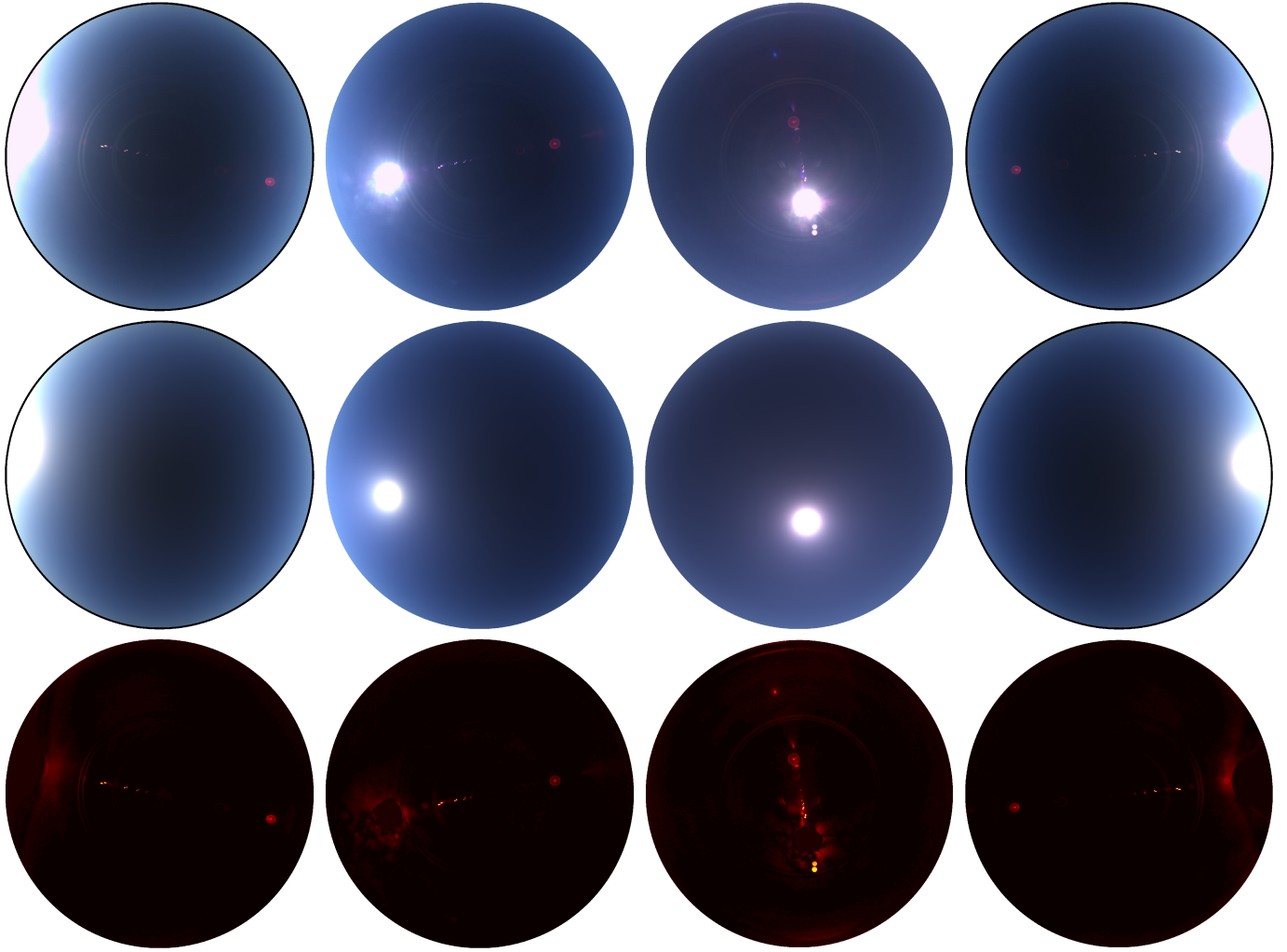


Figure 9: Real and generated clear-sky images and the absolute difference between them: the errors are mainly due to lens flare, blooming effects and soiling of the dome.

soiling of the dome because such errors are precisely located on the image, unlike the other sources of errors. A few examples of real and generated clear-sky images are given (Figure 9) and it can be observed that the generated clear-sky images reproduce fairly well the images taken with our sky imager, for the four solar elevations illustrated (similar results are obtained for all solar elevations). As expected, the error is mainly due to artifacts and soiling. Apart from these local errors, the absolute difference between the two images does not seem to be very dependent on PZA neither on SPA. To conclude this sub-section, we can say that both Eqs. (14) and (17) are able to reproduce at any solar zenith angle the pixels' clear-sky distribution accurately. However, the new formulation (Eq. (17)) outperforms the standard formulation (Eq. (14)) on the 2279 images tested, especially in the circumsolar area. Studies on a couple of other days have led to similar conclusions.

5.3. Application to cloud detection

As mentioned in Section 2.3, the single scattering assumption strongly simplifies the interaction between clouds and sunbeams. In the previous sections, no clouds were polluting the clear-sky

pattern. This section aims at evaluating the applicability of the proposed method to sky images with clouds.

An example of a clear-sky image generated from a cloudy sky image is provided on Figure 10. As we can see, parts of I_p^* are missing, especially near the Sun, due to the presence of clouds. Nevertheless, the map has enough points for the fit to succeed and the clear-sky image to be generated. Once the clear-sky image is generated, it can be used as a reference to assist the cloud detection algorithm. The absolute difference and absolute NRBR difference between the real image and the generated clear-sky one are shown on Figure 11. As it can be seen, the Sun is not apparent anymore whereas circumsolar clouds are still well defined. A simple thresholding technique can then be applied on the resulting image in order to accurately separate clouds from clear-sky elements. Note that a fixed threshold should be enough since removing the clear-sky background on images allows to greatly reduce the clear-sky intensity fluctuations produced by atmospheric particles over time.

As one can expect, the proposed method does not succeed in all cloudy conditions. In Figure 12 is plotted the success rate of the clear-sky image generation versus the percentage of clouds.

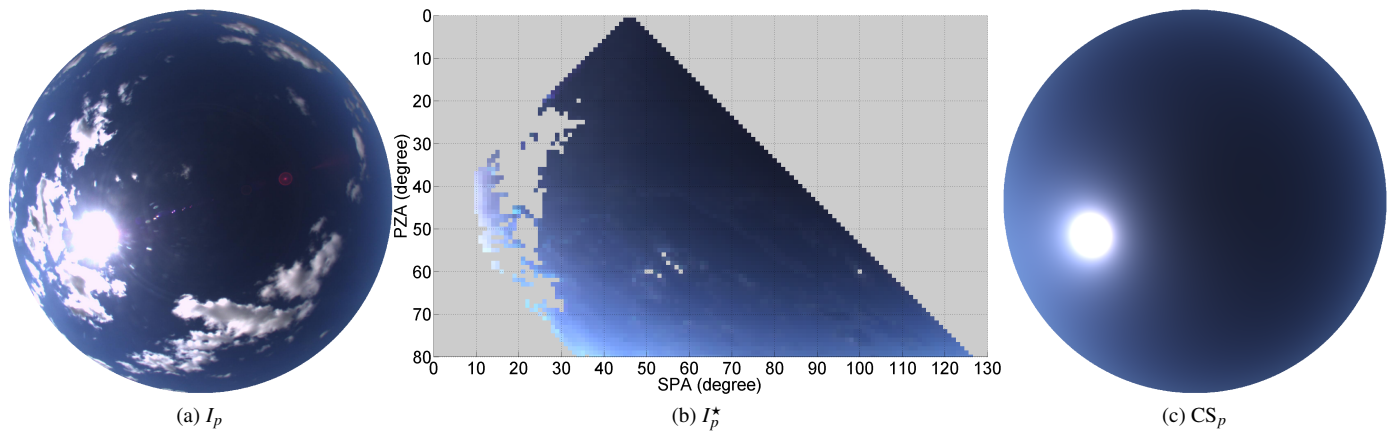


Figure 10: A cloudy sky image and its corresponding clear-sky image.

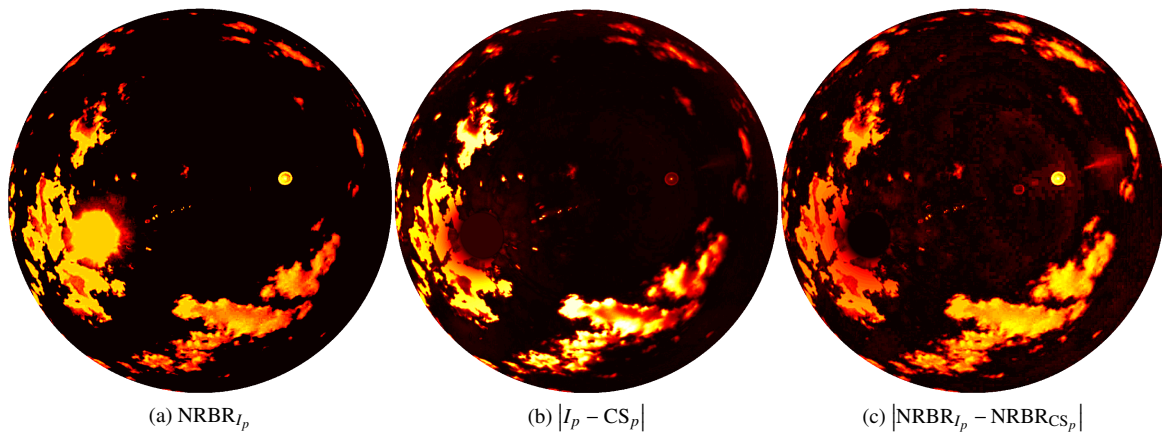


Figure 11: Absolute difference and absolute NRBR difference between the real image and the generated clear-sky one.

It can be seen that, when the cloud cover increases, the algorithm fails more and more frequently to find a unique smooth representation of the clear-sky background. Above 40% of clouds in the sky vault, the algorithm success rate falls down to less than 10%. However, when the cloud cover is high, two important things must be remembered. Firstly, in such conditions, using a generated clear-sky image to facilitate cloud detection becomes less necessary. Secondly, if the cloud cover is really high, it is unlikely that a CSP plant even operates. In other words, the plant operation strategy becomes very straightforward and then the cloud detection algorithm is pointless. In addition to the cloud cover, we found that the success rate of the algorithm is dependent on the distribution of clouds. For instance, broken clouds influence more the clear-sky radiance distribution than only one heavy cloud, at similar cloud cover. Nonetheless, as it can be seen on Figure 10, the clear-sky anisotropy is fairly well represented in case of a low cloud cover. Further tests showed that the results obtained when the cloud cover is not too high (typically below 40%) are satisfying and attest that simple empirical models are good enough to be used for our application.

REMARK

The results are specific to our camera and to the weather conditions prevailing in Perpignan, France. In a more turbid at-

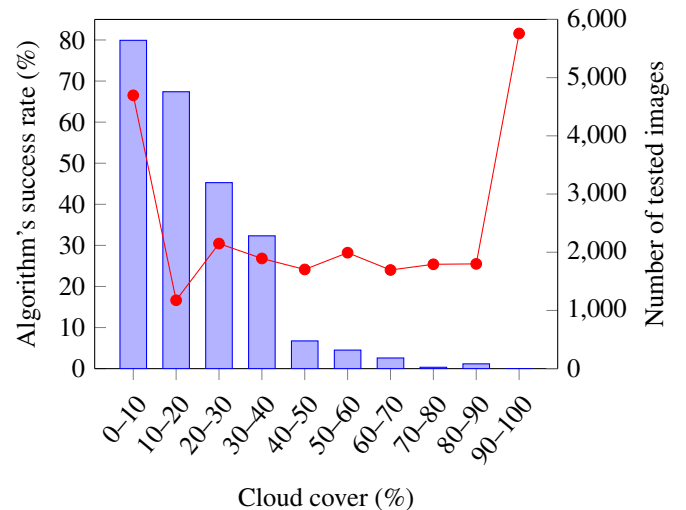


Figure 12: Success rate of the clear-sky image generation, depending on the percentage of clouds.

mosphere, the results could be less satisfying and the single scattering approximation would not be acceptable anymore. Nevertheless, in a very turbid atmosphere, differentiating clouds from clear-sky based on the visible spectrum may be hardly feasible. Therefore, regardless of the accuracy of the clear-sky

radiance distribution, the cloud detection algorithm would not be able to operate correctly in such conditions. ■

6. Conclusion and outlook

The main contribution of the present work lies in the development of an algorithm able to generate real-time clear-sky images from original sky images. This algorithm allows the background non-uniformity to be removed and can be used to facilitate cloud detection. First, a review of the existing models dealing with the sky radiance and luminance distributions has been done. It has shown that both distributions can be expressed using the same equation: a function of the sky element zenith angle and the angle between this sky element and the Sun. In addition, several studies about using a sky imager in order to measure these distributions has been presented. They demonstrated the feasibility of measuring sky radiance using a sky imager. A review of the existing sky imagers and their applications has been discussed and the setting of our system has been detailed. The calibration process, essential for evaluating the radiance distribution, has also been described.

After introducing the state-of-the-art as well as our experimental setup, a new formulation of the pixels intensity distribution has been presented. On the one hand, the relationship between sky radiance and pixels' intensity has been provided, according to the assumptions made. This relationship allowed the existing empirical models to be used on pixels intensity. On the other hand, a new empirical formulation, which aims at improving the pixel's intensity distribution in the circumsolar area, has been developed. It relies on experimental observations of the radiance profile near the Sun. The new formulation and the standard one have been then tested and compared using a set of clear-sky images. Both formulations showed a good ability to reproduce the clear-sky anisotropy. Nevertheless, the new formulation tends to be more accurate, especially near the Sun where it outperforms the standard formulation by 20%. As a consequence, this new formulation is selected as the starting point of our cloud detection algorithm. Finally, the methodology for cloud detection purpose is introduced and put forward the feasibility of generating clear-sky images from various types of sky images.

A study is ongoing to evaluate the new formulation using another camera and other places with different atmospheric conditions, *i.e.* different aerosols loads. Furthermore, high dynamic range imaging is under development in order to improve the sky visibility near the Sun. Such images could validate even more the new formulation since more information would be available in the circumsolar area. Finally, a database containing the coefficients of the new formulation and irradiance measurements is being set up. These coefficients are expected to exhibit a strong correlation with classical parameters like direct normal irradiance or air mass.

Acknowledgements

This work is part of the European project CSPIMP (Concentrated Solar Power efficiency IMProvement), initiated in 2013,

including GE Thermodyn, GE Nuovo Pignone, Acciona Energía, ARTS, and PROMES-CNRS.

References

- Adamson, D., December 1975. The role of multiple scattering in one-dimensional radiative transfer. Tech. rep., National Aeronautics and Space Administration.
- Blanc, P., Wald, L., Oct. 2012. The SG2 algorithm for a fast and accurate computation of the position of the Sun for multi-decadal time period. *Solar Energy* 86 (10), 3072–3083.
- Brunner, A. P., Hooper, F. C., Jul. 1993. Anisotropic sky radiance model based on narrow field of view measurements of shortwave radiance. *Solar Energy* 51 (1), 53–64.
- Buie, D., Monger, A. G., Dey, C. J., 2003. Sunshape distributions for terrestrial solar simulations. *Solar Energy* 74, 113–122.
- Cazorla Cabrera, A., 2010. Development of a sky imager for cloud classification and aerosol characterization. Ph.D. thesis, Universidad de Granada.
- CIE, 1994. CIE 108-1994 Guide to recommended practice of daylight measurement. Tech. rep., Commission internationale de l'éclairage.
- CIE, 2003. Spatial distribution of daylight - CIE standard general sky. Tech. rep., Commission internationale de l'éclairage.
- Dubovik, O., King, M. D., Aug. 2000. A flexible inversion algorithm for retrieval of aerosol optical properties from sun and sky radiance measurements. *Journal of Geophysical Research* 105 (D16), 20673–20696.
- Eissa, Y., Blanc, P., Oumbe, A., Ghedira, H., Wald, L., 2014. Estimation of the circumsolar ratio in a turbid atmosphere. *Energy Procedia* 57, 1169–1178.
- Ferraro, V., Mele, M., Marinelli, V., Jan. 2012. Analysis of sky luminance experimental data and comparison with calculation methods. *Energy* 37 (1), 287–298.
- Grether, D., Evans, D., Hunt, A., Whalig, M., 1980. Measurements and Analysis of Circumsolar Radiation. Tech. rep., Lawrence Berkeley National Laboratory, Berkeley.
- Gueymard, C. A., 1986. Une paramétrisation de la luminance énergétique du ciel clair en fonction de la turbidité. *Atmosphère-Océan* 24 (1), 1–15.
- Gueymard, C. A., Dec. 2012. Temporal variability in direct and global irradiance at various time scales as affected by aerosols. *Solar Energy* 86 (12), 3544–3553.
- Harrison, A., Jan. 1991. Directional sky luminance versus cloud cover and solar position. *Solar Energy* 46 (1), 13–19.
- Harrison, A., Coombes, C., 1988. Angular distribution of clear sky short wavelength radiance. *Solar Energy* 40 (1), 57–63.
- Heschong, L., 2002. Daylighting and Human Performance. *ASHRAE* 44 (6), 65–67.
- Igawa, N., Jul. 2014. Improving the All Sky Model for the luminance and radiance distributions of the sky. *Solar Energy* 105, 354–372.
- Igawa, N., Koga, Y., Matsuzawa, T., Nakamura, H., Jan. 2004. Models of sky radiance distribution and sky luminance distribution. *Solar Energy* 77 (2), 137–157.
- Juan, H., Da-Ren, L., 2009. Calibration and validation of an all-sky imager. *Journal of Atmospheric and Oceanic Science* 2 (4), 220–223.
- Kalapatapu, R., Chiesa, M., Armstrong, P., Wilbert, S., 2012. Measurement of DNI Angular Distribution with a Sunshape Profiling Irradiometer. In: *SolarPACES 2012*. Marrakesch, Marokko.
- Kittler, R., Perez, R., Darula, S., 1997. A new generation of sky standards. In: *LuxEuropa*. Amsterdam, pp. 359–373.
- Kittler, R., Perez, R., Darula, S., 1998. A set of standard skies characterizing daylight conditions for computer and energy conscious design. Tech. rep.
- Kocifaj, M., Oct. 2009. Sky luminance/radiance model with multiple scattering effect. *Solar Energy* 83 (10), 1914–1922.
- Kocifaj, M., 2012. Angular distribution of scattered radiation under broken cloud arrays: an approximation of successive orders of scattering. *Solar Energy* 86 (12), 3575–3586.
- Kocifaj, M., 2015. Unified model of radiance patterns under arbitrary sky conditions. *Solar Energy* 115, 40–51.
- Lehar, M., Glicksman, L., Aug. 2007. Rapid algorithm for modeling daylight distributions in office buildings. *Building and Environment* 42 (8), 2908–2919.
- Li, Q., Lu, W., Yang, J., Oct. 2011. A Hybrid Thresholding Algorithm for Cloud Detection on Ground-Based Color Images. *Journal of Atmospheric and Oceanic Technology* 28 (10), 1286–1296.

- Liang, S., Lewis, P., 1996. A parametric radiative transfer model for sky radiance distribution. *Journal of Quantitative Spectroscopy and Radiative Transfer* 55 (2), 181–189.
- Long, C. N., Sabburg, J. M., Calbó, J., Pagès, D., May 2006. Retrieving Cloud Characteristics from Ground-Based Daytime Color All-Sky Images. *Journal of Atmospheric and Oceanic Technology* 23 (5), 633–652.
- Mardaljevic, J., 2008. Sky model blends for predicting internal illuminance: a comparison founded on the BRE-IDMP dataset. *Journal of Building Performance Simulation* 1 (3), 163–173.
- Marquez, R., Coimbra, C. F., 2011. Forecasting of global and direct solar irradiance using stochastic learning methods, ground experiments and the {NWS} database. *Solar Energy* 85 (5), 746–756.
- Miyamoto, K., August 1964. Fish eye lens. *Journal of the Optical Society of America* 54 (8), 1060–1061.
- Neumann, A., von der Au, B., 1997. Sunshape Measurements at the DLR Solar Furnace Site in Cologne, Germany. In: *Solar Energy Forum*, ASME, Washington D.C., USA, p. 163.
- Olmo, F., Quirantes, A., Lara, V., Lyamani, H., Alados-Arboledas, L., May 2008. Aerosol optical properties assessed by an inversion method using the solar principal plane for non-spherical particles. *Journal of Quantitative Spectroscopy and Radiative Transfer* 109 (8), 1504–1516.
- Perez, R., Ineichen, P., Seals, R., Michalsky, J., Stewart, R., Jan. 1990. Modeling daylight availability and irradiance components from direct and global irradiance. *Solar Energy* 44 (5), 271–289.
- Perez, R., Seals, R., Michalsky, J., Sciences, A., 1993. All-weather model for sky luminance distribution - preliminary configuration and validation. *Solar Energy* 50, 235–245.
- Perez, R., Stewart, R., Scott, J. T., 1983. A two-parameter description of the sky hemisphere. In: *Fifth Conference on Atmospheric Radiation*. Baltimore, pp. 322–325.
- Pfister, G., McKenzie, R., Liley, J., Thomas, A., Forgan, B., Long, C., 2003. Cloud Coverage Based on All-Sky Imaging and Its Impact on Surface Solar Irradiance. *Journal of Applied Meteorology* 42 (10), 1421–1434.
- Reinhart, C. F., Walkenhorst, O., 2001. Validation of dynamic RADIANCE-based daylight simulations for a test office with external blinds. *Energy and Buildings* 33 (7), 683–697.
- Román, R., Antón, M., Cazorla, a., de Miguel, a., Olmo, F. J., Bilbao, J., Alados-Arboledas, L., Aug. 2012. Calibration of an all-sky camera for obtaining sky radiance at three wavelengths. *Atmospheric Measurement Techniques* 5 (8), 2013–2024.
- Rossini, E. G., Krenzinger, A., Nov. 2007. Maps of sky relative radiance and luminance distributions acquired with a monochromatic CCD camera. *Solar Energy* 81 (11), 1323–1332.
- Scaramuzza, D., Martinelli, A., Siegwart, R., Oct. 2006. A Toolbox for Easily Calibrating Omnidirectional Cameras. In: *2006 IEEE/RSJ International Conference on Intelligent Robots and Systems*. Ieee, pp. 5695–5701.
- Shields, J. E., Karr, M. E., Johnson, R. W., Burden, A. R., Mar. 2013. Day/night whole sky imagers for 24-h cloud and sky assessment: history and overview. *Applied optics* 52 (8), 1605–1616.
- Siala, F., Hooper, F., Jan. 1990. A model for the directional distribution of the diffuse sky radiance with an application to a CPC collector. *Solar Energy* 44 (5), 291–296.
- Smith, W. J., 2000. *Modern optical engineering: the design of optical systems*. McGraw-Hill.
- Steven, M., 1977. Standard distributions of clear sky radiance. *Quarterly Journal of the Royal Meteorological Society* 103 (437), 457–465.
- Tohsing, K., Schrempf, M., Riechelmann, S., Schilke, H., Seckmeyer, G., Mar. 2013. Measuring high-resolution sky luminance distributions with a CCD camera. *Applied optics* 52 (8), 1564–73.
- Tohsing, K., Schrempf, M., Riechelmann, S., Seckmeyer, G., Jul. 2014. Validation of spectral sky radiance derived from all-sky camera images – a case study. *Atmospheric Measurement Techniques* 7 (7), 2137–2146.
- van Bommel, W., van den Beld, G., Dec. 2004. Lighting for work: a review of visual and biological effects. *Lighting Research and Technology* 36 (4), 255–269.
- Van de Hulst, H. C., 1980. *Multiple light scattering*. Vol. 1. Academic Press.
- Vartiainen, E., May 2000. A new approach to estimating the diffuse irradiance on inclined surfaces. *Renewable Energy* 20 (1), 45–64.
- Vartiainen, E., Jan. 2001. Electricity benefits of daylighting and photovoltaics for various solar facade layouts in office buildings. *Energy and Buildings* 33 (2), 113–120.
- Voss, K. J., Zibordi, G., 1989. Radiometric and geometric calibration of a visible spectral electro-optic "fish-eye" camera radiance distribution system. *Journal of Atmospheric and Oceanic Technology* 6, 652–662.
- Wilbert, S., Reinhardt, B., DeVore, J., Röger, M., Pitz-Paal, R., Gueymard, C., Buras, R., Jun. 2013. Measurement of solar radiance profiles with the sun and aureole measurement system. *Journal of Solar Energy Engineering* 135 (4), 041002.
- Yang, H., Kurtz, B., Nguyen, D., Urquhart, B., Chow, C. W., Ghoniya, M., Kleissl, J., May 2014. Solar irradiance forecasting using a ground-based sky imager developed at UC San Diego. *Solar Energy* 103, 502–524.